

# Structure and Biocompatibility of Bioabsorbable Nanocomposites of Aliphatic-Aromatic Copolyester and Cellulose Nanocrystals

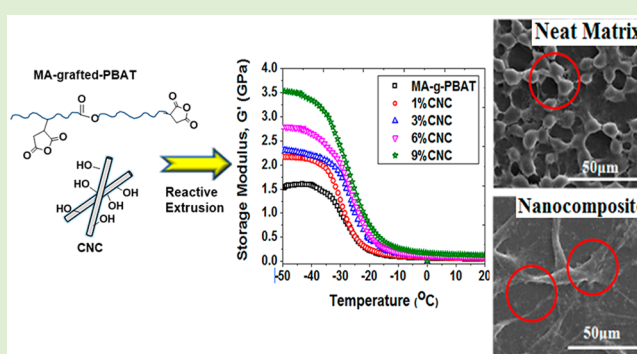
Shahab Kashani Rahimi,<sup>†</sup> Robabeh Aeinehvand,<sup>‡</sup> Kyoungtae Kim,<sup>†</sup> and Joshua U Otaigbe<sup>\*,†</sup>

<sup>†</sup>School of Polymers and High Performance Materials, The University of Southern Mississippi, 118 College Drive, Hattiesburg, Mississippi, United States

<sup>‡</sup>Nano-Biopolymers Research Laboratory, Department of Chemical Engineering, College of Engineering, University of Tehran, P.O. Box 11155-4563, Tehran, Iran

## S Supporting Information

**ABSTRACT:** Poly(butylene adipate-co-terephthalate) (PBAT) was first chemically modified via free radical grafting with maleic anhydride (MA) and the MA-g-PBAT graft copolymer was then used as a matrix material to obtain cellulose nanocrystal (CNC)-reinforced MA-g-PBAT bionanocomposites via reactive extrusion process to accelerate efforts to develop functional bioabsorbable polymer nanocomposites with improved properties. The molecular structure of the PBAT after chemical modification with maleic anhydride was confirmed by <sup>1</sup>H NMR and FTIR spectroscopy. The morphological observation of the nanocomposites revealed that the CNCs were finely dispersed in the matrix. Thermal analysis of the hybrids showed an improvement of the thermal stability of the nanocomposites upon increasing the CNC content. In addition, it was found that the CNC nucleated crystallization of the PBAT in the nanocomposites. Extensive melt rheological characterization of the nanocomposite samples revealed a significant improvement of the viscoelastic properties of the matrix due to the strong interfacial adhesion of the CNC particles to the PBAT. Further, development of the nonterminal characteristics of the viscoelastic material functions and exhibition of yield stress were correlated with the evolution of a 3D-network nanostructure of CNCs in the matrix. This CNC nanostructure was interpreted in the framework of scaling theory of fractal elastic gels, and found to be consistent with the structure of open-porous flocs. Tensile testing of the samples showed considerable improvement in the modulus and ultimate strength of the samples with increasing the CNC content. In addition, a positive shift of the glass transition temperature was found in dynamic mechanical analysis. Finally, in vitro biocompatibility using Thiazolyl blue tetrazolium bromide (MTT) assay and cell adhesion studies with L929 fibroblast cells revealed no cytotoxic effect of CNCs, confirming the biocompatibility of the nanocomposites and the associated significant improvement of cell adhesion, suggesting the potential applicability of this nanocomposite in biomedical and tissue engineering applications.



## 1. INTRODUCTION

Cellulose nanocrystals (CNCs) are among the most interesting biobased materials with exceptional structural properties such as high stiffness and axial elastic modulus of up to 150 GPa, lower density compared to that of silicates, high surface area with optimal benefits like design of various prescribed surface functionalities, and complete biodegradability after their useful service life.<sup>1,2</sup> Consequently, these highly crystalline rod-like nanoparticles (or cellulose “whiskers”) are finding a number of uses in different applications such as reinforcing fillers in various polymer composites,<sup>3</sup> rheology modifiers and colloidal additives,<sup>4</sup> antimicrobial additives,<sup>5</sup> additives for gas barrier improvement,<sup>6</sup> and synthesis platform for rational design of functional materials.<sup>7</sup>

The processing of the CNC-based nanocomposite materials normally involves a number of different techniques such as solvent casting which involves the dispersion of CNC in mostly

aqueous<sup>8</sup> or organic solvents,<sup>9</sup> followed by mixing with the host soluble polymer and subsequent final casting, in situ polymerization,<sup>10</sup> and melt extrusion.<sup>11</sup> It is worthy to note that, regardless of the process used in the preparation of CNC nanocomposites, the ultimate mechanical and structural properties of the nanocomposites are dictated by the microstructure and extent of dispersion of CNCs within the continuous polymer matrix. Development of a 3D percolated network of whiskers within the matrix polymer has been shown to significantly increase the physical properties of the polymer which normally occurs above the nanofiller percolation threshold.<sup>12</sup> The development of the network structure is facilitated by the strong intraparticle hydrogen bonding of the

Received: April 21, 2017

Revised: June 7, 2017

Published: June 15, 2017

CNCs, therefore, a highly dispersed physical state promotes the network formation by increasing the surface area of the particles. The formation of this nanofiller percolated network structure has been reported in a number of different matrix polymers such as acrylic latex,<sup>13</sup> polyurethane,<sup>14</sup> PVA,<sup>15</sup> and sodium caseinate.<sup>16</sup> In addition, a strong interfacial adhesion between the polar matrices and CNC surface hydroxyl groups have been reported to promote the development of a constrained rigid interphase that results in significant enhancement of mechanical properties even at very low CNC content compared to the percolation threshold. For example, Tang et al.<sup>17</sup> studied the reinforcing role of the CNCs within an epoxy matrix prepared via solvent casting. The significant enhancement of tensile modulus observed in the system was attributed by the authors just mentioned to the formation of a whisker-bound polymer layer that could effectively increase the volume fraction of “rigid” phase, thus, resulting in tensile modulus values that are significantly higher than that predicted by the percolation model. This strong interfacial adhesion and presence of the rigid interfacial polymer layer which was described by Narin<sup>2</sup> as “better than perfect” interface is crucial in achieving the maximum reinforcing effect of CNCs in polymer matrix.

In addition to naturally derived materials, synthetic biopolymers have also been the subject of extensive research and development due to a number of advantageous properties compared to that of their natural counterparts such as enhanced functionality, better processability and tunable inherent biodegradability.<sup>18</sup> In this context, poly(butylene adipate-co-terephthalate) or PBAT is an aromatic–aliphatic copolyester having a combination of the biodegradability of aliphatic polyesters and structural properties of aromatic polyesters at optimal aliphatic-aromatic ratio of 35–55% mol of aromatic units.<sup>19</sup> PBAT is a commercially available semicrystalline biodegradable thermoplastic used in a number of industrial applications such as extrudable plastic films for mulch and greenhouse film and packaging applications<sup>20,21</sup> and, more recently, found a number of uses in biomedical and tissue engineering due to its inherent biocompatibility.<sup>22</sup> In spite of these interesting properties, there are some drawbacks associated with properties of PBAT copolymer such as poor mechanical properties (especially for biomedical applications) and low thermal stability. Therefore, various strategies have been proposed to improve these limitations. One approach is the blending of PBAT with other biodegradable polyesters with better mechanical properties and, in particular, poly(lactic acid) (or PLA) to take advantage of the high modulus of PLA while retaining higher elongation at break and toughness imparted by PBAT.<sup>23</sup> Another approach is application of nanoadditives such as layered silicates,<sup>24</sup> carbon nanotubes,<sup>25</sup> and graphene.<sup>26</sup> Addition of up to 10 wt % neat montmorillonite clay and organically modified clay to PBAT, prepared via melt intercalation,<sup>27,28</sup> was shown to improve the mechanical properties of the PBAT, while further improvements could be achieved by the use of organically modified clay due to better particle dispersion.

Although use of biobased high performance reinforcing additives such as cellulose nanocrystals in PBAT matrix is of interest due to the biodegradable and eco-friendliness of the matrix and the reinforcement phases, its practical application is a challenging task due to the hydrophobic nature of PBAT and highly hydrophilic nature of cellulosic fibers. Development of CNC-reinforced PBAT system has been little studied in detail.

Only recently, Zhang et al.<sup>28</sup> reported the effect of addition of surface acetylated CNC into PBAT matrix. Their results showed that, although some improvement could be achieved by hydrophobization of the CNC through the modification of CNC surface with acetyl group, this improvement in properties was moderate and only small volume fractions of CNC (up to 2%) was used due to the difficulty in achieving effective CNC dispersion at high CNC concentrations. In fact, the modification of the CNC surface, imparts partial compatibility between the acetylated-CNC and PBAT. However, due to the lack of strong interfacial adhesion, the true potential of CNCs as reinforcement could not be achieved.

The current study is part of a long-range research program on development of functional biocompatible and bioabsorbable polymer nanocomposites with prescribed macromolecular structure and biological function in biomedical and tissue engineering applications. Here, we report an alternative approach of modifying the PBAT matrix with reactive maleic anhydride groups (MA-g-PBAT) in order to provide an opportunity for optimal chemical bond formation at the interface of CNC and PBAT. The current article describes an extensive investigation of the MA-g-PBAT/CNC nanocomposites at higher CNC concentrations with a focus on development of functional CNC microstructure within the PBAT matrix, and the associated effects on mechanical, rheological and thermal properties of the nanocomposites. In addition, the biocompatibility of the obtained fully biodegradable nanocomposites via *in vitro* tests is reported in order to provide a better understanding of the prescribed macromolecular structure and biological function in potential uses in biomedical and tissue engineering.

## 2. EXPERIMENTAL SECTION

**2.1. Materials and Sample Preparation.** The PBAT polymer used was an Ecoflex C1200 grade (purchased from BASF) with melt flow index (MFI) of 2.5–4.5 (at 190 °C; 2.16 kg), density of  $1.26 \pm 0.01$  g/cm<sup>3</sup>, and melting point of  $115 \pm 5$  °C. Maleic anhydride (MA) and benzoyl peroxide (BPO, radical initiator) were purchased from Aldrich and used without further purification. Modification of PBAT with MA was carried out according to the method reported by Nabar et al.<sup>29</sup> with the following modifications. In a round-bottom flask, a masterbatch of PBAT containing the MA were prepared as follows: Desired amount of fully dried PBAT was dissolved in chloroform already purged with dry nitrogen followed by addition of the MA, and the resulting solution was mixed for 1 h under an inert atmosphere. Finally, the solution was poured in a Teflon Petri dish and kept under reduced pressure (under dry nitrogen) until the solvent was evaporated. Similarly, in a separate flask a masterbatch of the PBAT containing the BPO was prepared. Preparation of MA-g-PBAT was carried out by melt processing of PBAT granules and the two masterbatches containing the MA and BPO with a total MA content of 5 wt % and BPO content of 0.5 wt % in a Thermo Haake Polydrive internal mixer for 8 min at 185 °C using a rotor speed of 80 rpm. Subsequently, the MA-g-PBAT was taken out and quenched in liquid nitrogen and granulated into small pieces for further analysis and a second melt processing step with CNC.

The extent of MA grafting was measured using titration following the protocol described previously.<sup>29</sup> First, the unreacted MA of the sample was removed by drying the granulated sample in a vacuum oven at 90 °C overnight to constant weight. Next, a 0.01 g/mL solution of MA-g-PBAT in chloroform was prepared followed by 30 min of mixing with 1 mL of 1 M hydrochloric acid in order to hydrolyze the anhydride groups to carboxylic acid. The MA-g-PBAT (with hydrolyzed MA groups) was recovered by precipitation in methanol, filtration, and drying at 90 °C. Subsequently, a solution of purified MA-g-PBAT was titrated with a methanolic solution of

potassium hydroxide (KOH) to phenolphthalein end point. The grafted MA content was calculated using the following equation:

$$\% \text{grafted MA} = \frac{0.5V_{\text{KOH}}N_{\text{KOH}}}{W_{\text{sample}}} \times 98.06 \times 100 \quad (1)$$

where the  $N$  and  $V$  are respectively normality and volume (per liter) of KOH and  $W$  is the mass of the MA-g-PBAT sample in grams. The MA grafted content was found to be 0.92%.

The cellulose nanocrystals were prepared using the sulfuric acid hydrolysis of bleached cellulose pulp as described in our previous publication.<sup>30</sup> The CNC surface sulfate groups were neutralized by NaOH solution to form sodium sulfate groups followed by dialysis in distilled (DI) water to pH neutrality. The dispersion of CNC in DI water was sonicated and sprayed into agitating liquid nitrogen bath to form a slurry. The slurry was then freeze-dried to recover the CNCs (i.e., spray freeze-drying technique). This method of recovery results in relatively less CNC particle aggregation compared to that obtained from the conventional bulk freeze-drying technique. The characteristic properties of the CNCs prepared and used in this work are shown in Table 1. The concentration of surface sulfate groups was measured

**Table 1. Characteristic Properties of Cellulose Nanocrystals**

	length (nm)	diameter (nm)	aspect ratio	surface charge (mmol of $\text{OSO}_3^-$ /kg of CNC)
cellulose nanocrystals	$190 \pm 28$	$11 \pm 2$	$17.6 \pm 5$	$216 \pm 2$

using a conductometric titration method. About 10 mL of 5 mM NaCl solution was added to 50 mL of 0.01% CNC dispersion followed by titration with a 2 mM NaOH solution under continuous stirring. The conductivity of the dispersion was monitored with a Mettler Toledo SevenMulti instrument. The tests were repeated three times on freshly prepared samples and the following equation proposed by Dong and co-workers<sup>31</sup> was used to calculate the surface charge of the cellulose nanocrystals (in the form of  $\text{OSO}_3^-$ ):

$$S(\%) = \frac{32V \cdot C}{W \cdot w_t} \quad (2)$$

where the  $C$  and  $V$  are the concentration and volume of the titrant (NaOH),  $W$  is the weight of the suspension, and  $w_t$  is the weight fraction of CNC dispersion.

As shown in Table 1, the surface charge of the prepared cellulose nanocrystals is 215.6 mmol/kg of CNC which corresponds to the substitution degree of 0.69%.

The nanocomposite samples were prepared by reactive twin screw extrusion process. The granulated MA-g-PBAT was briefly washed with anhydrous acetone (to remove the majority of unreacted MA) and dried in a vacuum oven for at least 24 h at 90 °C to constant weight to remove the moisture and any remaining unreacted MA monomer. The polymer granules and cellulose powder were physically mixed and fed into a Thermo Haake Minilab microcompounder (corotating conical screws) in the recycle mode at 140 °C for 8 min at 120 rpm under a dried nitrogen atmosphere. Nanocomposites with 1, 3, 6, and 9 wt % of CNC were prepared and hereinafter referred to as “x%CNC” where “x” denotes the content of CNC in the nanocomposite sample. For comparison purpose, similar compositions of the nanocomposites were prepared using the pristine PBAT matrix (without MA modification) to analyze the effect of matrix modification on thermal and rheological properties.

**2.2. Chemical Structure and Molecular Mass Characterization.**  $^1\text{H}$  NMR spectra were obtained using a 300 MHz Varian Mercury plus NMR (VNMR 6.1C) spectrometer using  $\text{CDCl}_3$  as the solvent. Standard  $^1\text{H}$  pulse sequences were used, and all  $^1\text{H}$  chemical shifts were referenced to TMS (0 ppm).

Size exclusion chromatography (SEC) measurements were conducted on a GPC consisting of Waters Alliance 2695 separation module equipped with a multiangle laser light scattering (MALLS)

detector (miniDAWN TREOS, Wyatt Technology Inc.) and interferometric refractometer (T-rex, Wyatt Technology Inc.) using a freshly distilled tetrahydrofuran (or THF) as the mobile phase and polystyrene standards for calibration operating at 35 °C.

Attenuated total reflectance-infrared (ATR-IR) spectroscopy measurements were carried out on a Nicolet 6700 FT-IR spectrometer in the range of 4000–400  $\text{cm}^{-1}$  with a total number of 1028 scans with a resolution of 4  $\text{cm}^{-1}$ . Compression molded thin films of the samples were used for the IR analysis.

**2.3. Scanning and transmission electron microscopy (SEM and TEM).** SEM images were acquired using a Sigma field-emission scanning electron microscope (ZEISS, U.S.A.) using a 5 kV accelerating voltage. Images were taken from the smooth cryo-fractured surfaces sputter-coated with silver for enhanced conductivity. TEM image of the cellulose nanocrystals were obtained using a ZEISS EM10 transmission electron microscope at accelerating voltage of 50 kV. An aqueous dispersion of CNC in the concentration range of 0.1–0.3 wt % was prepared and a small drop was placed on a TEM copper grid for image acquisition. In order to obtain the TEM images of the 3% and 9% CNC nanocomposite samples, first a rectangular bar with dimensions of  $1.08 \times 14.90 \times 20 \text{ mm}^3$  were prepared by injection molding at 140 °C using a Dac microinjector. Then, a thin slice of the sample along the injection direction was cut and sandwiched between epoxy. Finally, thin slices of about 80–100 nm were cut from the epoxy-polymer sandwich using a Leica ultramicrotome with a diamond knife and placed on the copper grid for imaging.

**2.4. Thermal Analysis.** Thermogravimetric analysis (TGA) data were obtained on a Q500 TA Instruments TGA with a heating rate of 10 °C  $\text{min}^{-1}$  under a nitrogen atmosphere with a gas flow rate of 40  $\text{mL min}^{-1}$ . Samples (10–20 mg) were heated from room temperature up to 600 °C. Crystallization and melting behavior of the materials were studied using a TA Instruments Q100 DSC with a heating and cooling rate of 10 °C/min. A heat-cool-heat cycle in the temperature range of 25–180 °C was applied with the first heating run used to remove the thermal history of the samples. The crystallization during the cooling run and the subsequent melting data were acquired via DSC experiments that were conducted under a dry nitrogen atmosphere.

Dynamic mechanical properties of the MA-g-PBAT matrix and the nanocomposites were measured using a TA Instruments Q800 dynamic mechanical analyzer (DMA) in tension mode. Dynamic viscoelastic properties were measured in the range of –50 to 60 °C with a rate of 3 °C/min at a constant frequency of 1 Hz.

**2.5. Mechanical and Rheological Properties.** Tensile tests were performed on an Instron 5582 MTS tensile tester with a crosshead speed of 10 mm/min at room temperature. At least five injection molded dogbone shaped specimens with a span length of 28 mm were tested for each composition. Rheological experiments were conducted using an Anton Paar MCR501 shear rheometer using 25 mm parallel plate geometry at a temperature of 140 °C. Frequency sweep tests were performed in the 0.01–100 rad/s range with strain amplitude of 1% (which was found to be in the linear viscoelastic region in a prior strain sweep tests).

**2.6. Cell Culture and Cell Adhesion Tests.** The proliferation rates of fibroblast (i.e., L929) cells on the bionanocomposites were investigated via MTT assay which is a colorimetric assay for measuring the activity of cellular enzymes that reduce the tetrazolium dye, MTT, to its insoluble formazan, giving a purple color. First, a 96-well culture plate was selected for seeding of  $1.5 \times 10^4$  cells/ $\text{cm}^2$  using the culture medium of Dulbecco's modified Eagle's medium, DMEM (Gibco) + 10% Fetal Bovine Serum (Gibco) and supplemented with antibiotic–antimycotic solution (100  $\mu\text{g/mL}$  of each, Gibco). Samples of  $1 \times 1 \text{ cm}^2$  size were first sterilized for 45 min on each side with ultraviolet (UV) light (CNC was filtered through a 0.22  $\mu\text{m}$  PVDF syringe) and then in each well and incubated at 37 °C and 5%  $\text{CO}_2$  for 1 week. Subsequently, 1 mL of the extracted medium was added to the culture plates followed by 1, 2, and 3 days of incubation time. At selected times, the supernatant was removed from the cells culture medium and the cells were washed three times with phosphate buffered saline (PBS) solution to eliminate nonviable cells. A total of 100  $\mu\text{L}$  of MTT



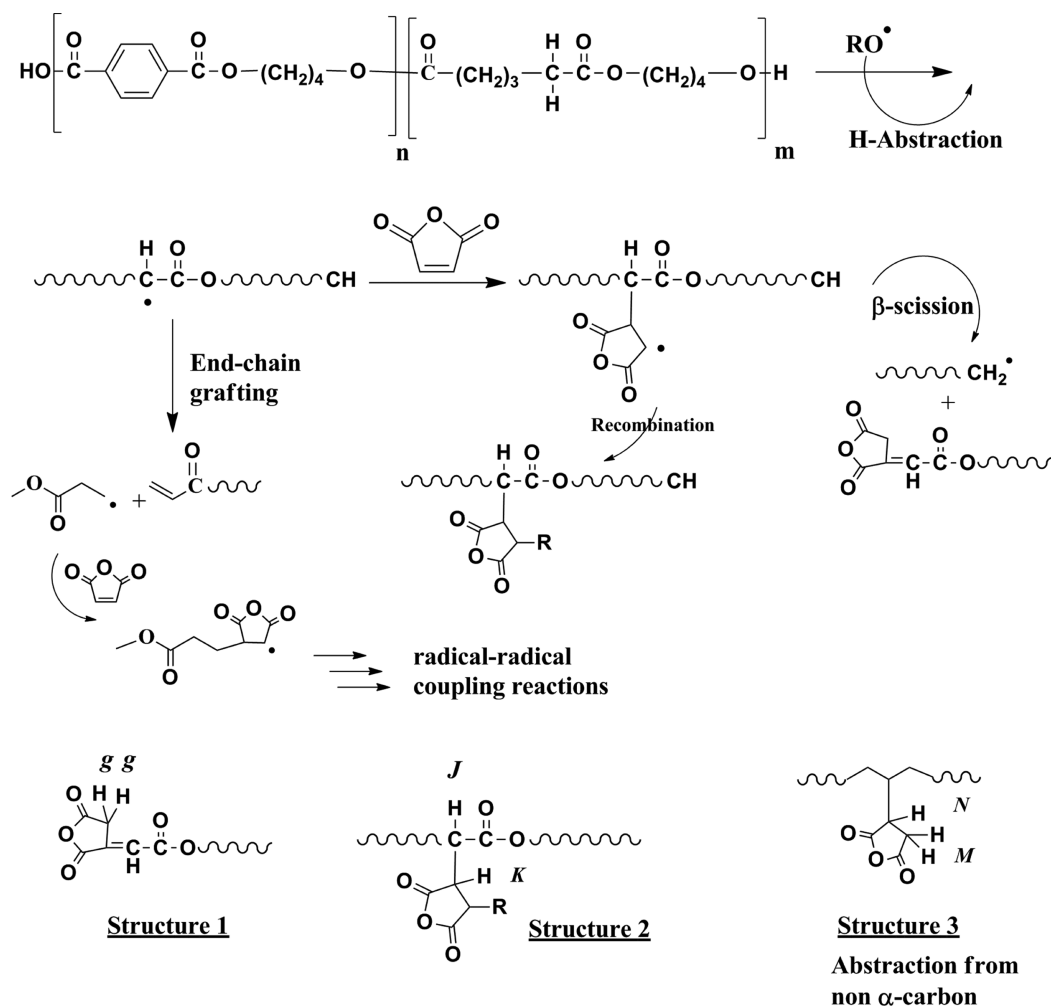


**Figure 1.** Reaction scheme showing the mechanism of MA grafting onto PBAT chains followed by subsequent termination routes.

solution (10 mg/mL in Dulbecco's modified Eagle medium) was added to each well. For conversion of MTT to formazan crystals by mitochondrial dehydrogenases of living cells, the plate was incubated at 37 °C for 4 h. After removing the culture media, 0.5 mL of isopropanol was added to each well followed by 20 min of shaking in incubator to allow total color release. The optical density was recorded at a wavelength of 570 nm in a microplate ELISA reader. The same procedure was performed for cells cultured on empty wells of the polystyrene culture medium as a control sample. The experiments were carried out in triplicate with the average results reported. The relative viability or cell growth (%) normalized by control group was calculated by the equation,  $[A]_s/[A]_c \times 100\%$ , where  $[A]_s$  is the absorbance of the cells with nanocomposites and  $[A]_c$  is the absorbance of the control cells.

In order to assess the cell adhesion, the sterilized thin films ( $1 \times 1 \text{ cm}^2$ ) of the MA-g-PBAT and 9%CNC samples were placed on a coverglass in a six-well plate and then pre-equilibrated with the culture medium for 12 h at 37 °C in a 5%  $\text{CO}_2$  atmosphere. Approximately  $15 \times 10^4$  cells were added to the medium and left for 4 h for adhesion. Subsequently, the culture medium was added to each individual well and followed by incubation for 72 h. After the 3 days incubation period, the supernatant was removed and the cells were washed with PBS and then were fixed by glutaraldehyde for 15 min. Finally, the glutaraldehyde was removed from the cells and the cells were respectively washed three times with phosphate-buffered saline (or PBS) solution and water and dried.

### 3. RESULTS AND DISCUSSION

**3.1. Chemical Structure and Molecular Mass Characterization.** The free radical grafting of maleic anhydride on PBAT follows a number of different reaction mechanisms which is depicted in Figure 1. The main mechanism of grafting has been suggested by some previous authors,<sup>29</sup> to be through the H-abstraction from the  $\alpha$ -carbon of the adipate segment due to the free radical stabilization effect of the carbonyl group. This is followed by chemical bond formation with the maleic anhydride group to form a succinic anhydride pendant on the PBAT chain. This free radical graft copolymerization reaction has been shown to undergo  $\beta$ -scission reaction splitting of the chain to yield a succinic anhydride end group. In addition, this anhydride free radical can abstract further hydrogens or couple (i.e., recombine) with other free radical moieties shown as "R" group in structure 2 of Figure 1. Another proposed mechanism<sup>32</sup> for maleic anhydride grafting onto polyesters is chain-end grafting based on the abstraction of the  $\alpha$ -carbon hydrogen followed by  $\beta$ -scission and formation of a vinylidene and macroradical chain ends. The macroradical chain ends can react with anhydride group (as shown in Figure 1) following a number of different paths to couple with other free radical moieties. It is worth noting that the  $\beta$ -scission is usually favored in melt processing while during the solution free radical reaction, coupling of radicals before scission is the dominating mechanism.<sup>33</sup> In addition, since the grafting reaction was



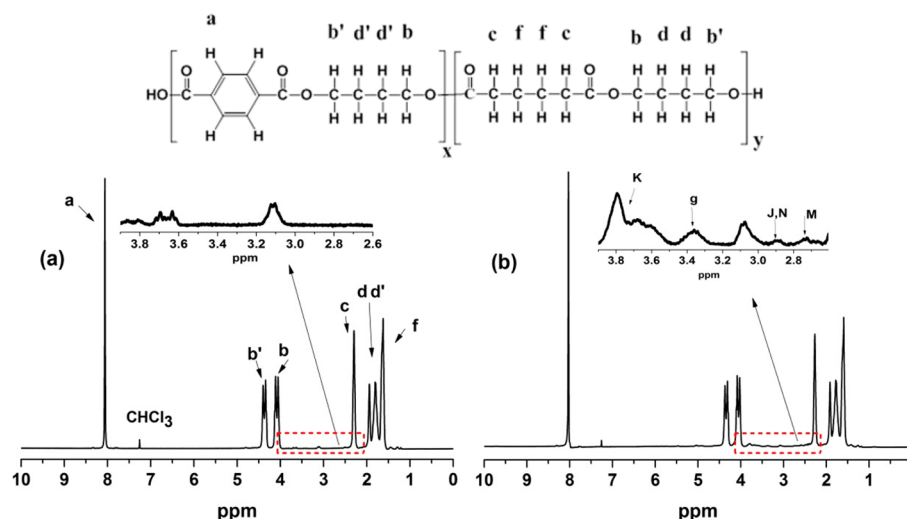


**Figure 2.**  $^1\text{H}$  NMR spectra of (a) PBAT and (b) MA-g-PBAT ( $\text{CDCl}_3$  solvent, 300 MHz).

carried out at the extrusion temperature of  $185^\circ\text{C}$ , homopolymerization of MA units are unlikely to occur.<sup>34,35</sup>

The  $^1\text{H}$  NMR spectra of PBAT and MA-g-PBAT are shown in Figure 2. The dominating protons of the both materials are depicted on the graphs. The resonance peaks observed at 1.6 ppm and 1.8–1.9 ppm correspond to *f*, *d*, and *d'* protons, respectively. The *c* protons appear at 2.3 ppm. The *b* protons showed up at 4.0–4.1 ppm while the peaks showing at 4.3–4.4 correspond to *b'* protons, respectively. The (*a*) protons of phenyl group are those at 8.03 ppm.

In order to further investigate the MA grafting reaction on PBAT by  $^1\text{H}$  NMR, the resonance range of 2.0–4.0 ppm is considered and shown in the insertion graphs of Figure 2. By comparing this with the spectrum of neat PBAT, the resonance at 3.3–3.4 ppm is attributed to the *g* protons of the structure 1 (see Figure 1). The peak at 2.9 ppm corresponds to the *J* proton of the  $\alpha$ -carbon attached to the MA unit. The evolution of this peak in the 3.7–3.8 ppm is attributed to the *K* type protons of the MA unit attached to the  $\alpha$ -carbon of the PBAT chain (structure 2).

In addition, it has been shown<sup>36</sup> that the MA units can abstract a proton from a non- $\alpha$  carbon of the polyolefins. In the case of PBAT, this could be carbons of terephthalate or butylene segments. The evidence of such grafting is in the  $^1\text{H}$  NMR peaks showing at 2.7 ppm which is attributed to the *M*-type protons (structure 3). The *N*-type proton is merged with the peak appearing at 2.9 ppm.

Further, the ATR-FTIR spectra of neat and MA-modified PBAT are presented in Figure 3. The major characteristic peaks of the PBAT are as follows:<sup>37,38</sup> stretching vibration of carbonyl group ( $\text{C}=\text{O}$ ) at  $1710\text{ cm}^{-1}$ , stretching vibration of ester bond ( $\text{C}-\text{O}$ ) at  $1105$  and  $1274\text{ cm}^{-1}$ , characteristic peaks of the phenylene group with stretching vibration at  $1390$ ,  $1400$ ,  $1456$ , and  $1510\text{ cm}^{-1}$ , planar bending vibration at  $735$  and  $1020\text{ cm}^{-1}$ , and the asymmetric stretching of the aliphatic  $-\text{CH}_2-$  groups at  $2955\text{ cm}^{-1}$ .

In the case of the MA-g-PBAT sample, in addition to the peak seen in the neat PBAT, there is a distinctive peak appearing at  $1855\text{ cm}^{-1}$  in addition to the broadening of the shoulder in the range of  $1710$ – $1750\text{ cm}^{-1}$ . These peaks are attributed to asymmetric and symmetric stretching vibration of  $\text{C}=\text{O}$  in the grafted succinic anhydride group, respectively. In addition, the peak at  $1660\text{ cm}^{-1}$  corresponds to stretching

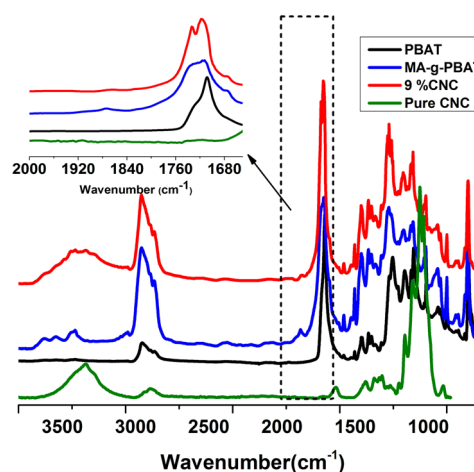


**Figure 3.** ATR-IR spectra of PBAT, MA-g-PBAT, and 9% CNC nanocomposites.

vibration of  $\text{C}=\text{C}$ , which is formed as already discussed above in the chain end grafting mechanism. The vibration of  $=\text{C}-\text{H}$  bond appears in the  $3000$ – $3100\text{ cm}^{-1}$ .

In the 9% nanocomposite sample, the evolution of a distinctive peak at  $1740\text{ cm}^{-1}$  is clearly evident. This peak has been attributed<sup>39</sup> to the formation of an ester bond resulting from transesterification reaction, which confirms the formation of the interfacial bond between the anhydride groups and the surface hydroxyl groups of the cellulose. The broad peak in the range of  $3100$ – $3600\text{ cm}^{-1}$  is assigned to the H-bonded stretching vibration of cellulose hydroxyls.

**3.2. Thermal and Dynamic Mechanical Properties.** The thermal stability of the MA-g-PBAT/CNC nanocomposites is shown in the TGA scans depicted in Figure 4 with the extracted values presented in Table 2. This figure shows that the MA-g-PBAT matrix undergoes a two-step degradation process. The first drop in the weight loss occurs around  $320^\circ\text{C}$  and the second major weight loss occurs at around  $400^\circ\text{C}$ . In the DTG curve shown in the insertion plot of Figure 4, this two-step thermal degradation process is clearly evident as two separate peaks showing the temperature at which the maximum thermal degradation occurs for each step. While the major weight loss occurring around  $400^\circ\text{C}$  is close to the values reported in

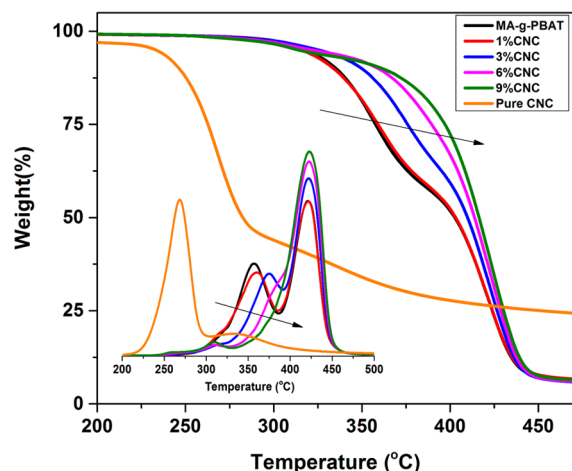


**Figure 4.** TGA and DTG curves for MA-g-PBAT/CNC nanocomposites.

**Table 2.** Results of TGA Experiment on the Nanocomposite Samples

	$T_{\text{onset}}$ (°C)	$T_{30\%}$ (°C)	$T_{70\%}$ (°C)	DTG peak 1 (°C)	DTG peak 2 (°C)
MA-g-PBAT	320.1	401.3	363.9	420.3	356.4
1%CNC	321.8	403.2	365.8	420.4	358.3
3%CNC	345.6	421.5	382.9	423.6	372.5
6%CNC	377.2	430.9	396.3	426.1	381.7
9%CNC	395.4	403.4	427.0	390.1	423.9

literature for PBAT polymer,<sup>28</sup> the lower degradation temperature observed in the current study is attributed to the chain branches and the broken chain segments during the melt processing.

Figure 4 also shows that, with addition of CNC particles, the first weight loss step gradually decreased and almost disappeared with the highest CNC concentration as evidenced by the shoulder (first minor weight loss) gradually moving toward higher temperatures. In fact, as shown in Table 1, the onset degradation temperature for the first step increased from 320 °C for the neat matrix to 395 °C for the 9%CNC nanocomposites. This increase is also observed for the second major weight loss step increasing from 401 °C for the neat matrix to 431 °C for the 6%CNC. This onset degradation temperature was not clearly detectable in the case of 9%CNC

because it increased to higher temperatures. The onset degradation temperature of maximum degradation rate (i.e., peaks of DTG curve) also undergo major shift toward higher temperatures with increasing CNC concentration. The shoulder peak increases from 356 °C for the matrix to 390 °C for the 9%CNC nanocomposite while the major DTG peak showed slight increase in the temperature.

The enhanced thermal stability of the nanocomposite systems was also implied by the temperature of residual weight at 70% and 30% mass. Clearly, with increasing CNC content, the temperature corresponding to 30 and 70% mass loss increased toward higher values. This enhancement of thermal stability is attributed to the formation of cross-linked segments upon interfacial reaction of MA units of PBAT with the surface hydroxyl groups of CNC. In fact, the cellulose nanocrystals act as cross-linkers binding the PBAT chains together that enhanced the thermal stability of polymer.

For comparison, the TGA plot of the unmodified PBAT/CNC nanocomposites (Figure S2 in Supporting Information) clearly shows that in the unmodified samples, the addition of CNC simply reduces the thermal stability of the nanocomposite following a rule of mixture trend. This clearly shows the effect of interfacial bond formation and compatibility on thermal stability of these hybrid materials.

The crystallization and melting behavior of the MA-g-PBAT/CNC nanocomposites were studied using DSC as already described. A heat-cool-heat program was used to first remove the thermal history of the samples followed by crystallization during cooling and subsequent heat run to study the melting behavior. The crystallization exotherms in the cool runs are shown in Figure 5a and the second heat runs (melting endotherms) are shown in Figure 5b. The extracted data are presented in Table 3. Clearly, the incorporation of the

**Table 3.** Crystallization and Melting Temperatures, the Enthalpy of Fusion, and Degree of Crystallinity for MA-g-PBAT Nanocomposites

	$T_c$ (°C)	$T_m$ (°C)	$\Delta H_m$ (J/g)	$\chi$ (%)
MA-g-PBAT	81.1 (0.6)	122.8 (0.1)	11.2 (0.3)	9.8
1%CNC	82.8 (0.1)	124.4 (0.3)	9.1 (0.3)	8.1
3%CNC	83.3 (0.2)	125.1 (0.4)	8.2 (0.4)	7.4
6%CNC	85.7 (0.5)	125.7 (0.1)	8.6 (0.1)	8.0
9%CNC	87.4 (0.3)	126.1 (0.5)	9.5 (0.2)	9.2

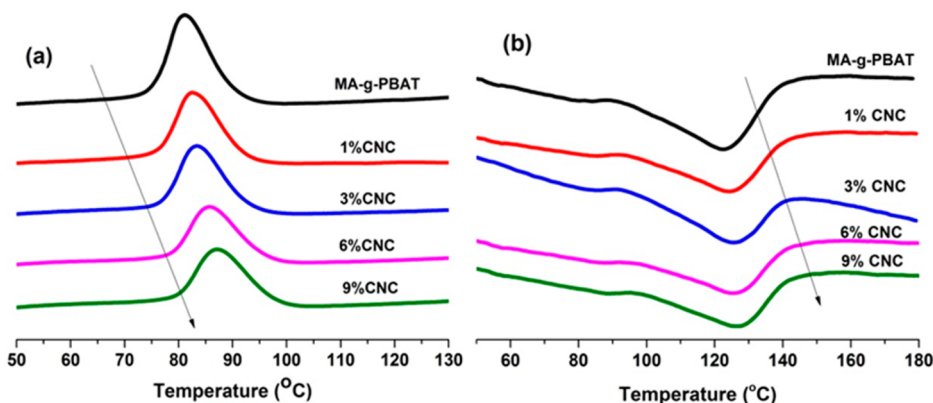


**Figure 5.** (a) Crystallization exotherms and (b) melting endotherms (second heat run) of the MA-g-PBAT/CNC nanocomposites.

nanocrystals in the MA-g-PBAT matrix showed that the crystallization temperature of the matrix gradually increased toward higher temperatures. The observed  $T_c$  of 81 °C increased to 87 °C with incorporation of CNC particles. This clearly shows that the presence of the cellulose whiskers gave a heterogeneous nucleation effect by increasing the nucleating sites for promotion of crystallization of the PBAT like other researchers have reported for a silica-reinforced PBAT systems<sup>28</sup> where silicate platelets provided nucleating sites for the polymer matrix crystallization. Cellulose whiskers have also been found to promote crystal nucleation in other polyester matrix nanocomposites such as PLA.<sup>40</sup>

In the second heating cycle (Figure 5b), it can be seen that while the pure PBAT showed an endothermic melting peak at 122 °C, with increasing content of cellulose nanocrystals, the melting temperatures showed a gradual increase up to the maximum temperature of 126 °C in the case of 9%CNC sample.

In order to obtain the degree of crystallinity ( $\chi_c$ ) of the nanocomposite samples, the heat of fusion of a 100% crystalline PBAT was calculated using the approach of Herrera et al.<sup>41</sup> that involves the contributions of methylene, *p*-phenylene, and ester linkages with values of 4.0, 5.0, and −2.5 kJ/mol, respectively, resulting in a final value of 114 J/g as the enthalpy of fusion of 100% crystalline PBAT. The absolute degrees of crystallinities were calculated using the following equation:

$$\chi_c(\%) = 100 \times \frac{\Delta H_m}{\Delta H_{100\%} \times (1 - x_w)} \quad (3)$$

where the  $\Delta H_m$  and  $x_w$  are, respectively, the experimental enthalpy of fusion and the weight content of the CNCs.

Based on the values obtained, it can be seen that the enthalpy of fusion initially decreased from 11.2 J/g to 9.1 and 8.2 J/g for the samples containing 1 and 3 wt % of the CNC particles, respectively. However, upon further increasing the CNC concentration, the  $\Delta H_m$  values increased again to 9.5 J/g but still remained lower than that of the neat MA-g-PBAT sample. Similarly, the degree of crystallinity decreased from 9.8% of the MA-g-PBAT matrix to 7.4% of the 3%CNC nanocomposite while it increased again with 6 and 9% of CNC back to 9.2%. Overall, it is believed that the presence of the cellulose nanocrystals inhibited the crystallization process of PBAT chains due to the polymer chain motion restriction and increasing viscosity of the matrix during the cooling process that, in turn, prevents sufficient crystal growth from occurring.

On the other hand, with higher CNC concentration (i.e.,  $\geq 6\%$ ), the heterogeneous nucleating effect of CNC on PBAT crystallization becomes more prominent. This nucleating effect partly offsets the crystal growth inhibition effect and, therefore, slightly increases the crystallinity content as observed in the samples. This increase is relative to the samples with 1 and 3% CNC, while the overall degree of crystallization still remains lower compared to that of the matrix (MA-g-PBAT) due to the restriction imposed by the CNCs on the chain flexibility of the interfacial polymer layer around the whiskers in the melt state as well as the physical barrier (due to the presence of CNC) against crystal growth. A similar behavior was reported for a system of poly(3-hydroxybutyrate-co-3-hydroxyvalerate) nanocomposite reinforced with CNC<sup>42</sup> where a dual effect of chain confinement together with heterogeneous nucleation due to the presence of cellulose whiskers was proposed.

The dynamic mechanical properties of the MA-g-PBAT matrix and the nanocomposites were evaluated using DMA and the obtained results are presented in Table 4. The variation of

**Table 4. Extracted Data from DMA Experiments**

	$E'_{-40\text{ }^\circ\text{C}}$ (GPa)	$E'_{20\text{ }^\circ\text{C}}$ (MPa)	$\tan \delta_{\max}$	peak $\tan \delta_{\max}$ (°C)
MA-g-PBAT	1.64 (0.12)	52.1 (4.1)	0.39	−24.3 (1.1)
1%CNC	2.12 (0.22)	65.5 (5.3)	0.37	−23.1 (0.9)
3%CNC	2.27 (0.18)	81.2 (2.4)	0.34	−21.3 (1.1)
6%CNC	2.75 (0.15)	95.5 (4.6)	0.32	−19.8 (1.2)
9%CNC	3.45 (0.21)	121.4 (4.5)	0.29	−17.3 (1.2)

the storage modulus ( $E'$ ) vs temperature is shown in Figure 6a. PBAT has two transition temperatures: the major transition is the glass transition temperature corresponding to linear butylene-adipate segments observed around −20 °C, while the second minor transition is due to the relaxation of the relatively stiffer terephthalate unit occurring around 35 °C. The variation of storage modulus versus temperature showed that upon increasing the CNC concentration, there is a significant increase in the modulus of the sample before the first transition temperature. For example, at a temperature of −40 °C, the storage modulus value increased from 1.64 to 3.45 GPa upon addition of 9% CNC. This strong reinforcing effect of cellulose nanocrystals is due to the strong interfacial adhesion by the chemical bond formation at the polymer–particle interface which facilitates the stress transfer to the stiff and highly elastic cellulose nanocrystals. Above the major glass transition temperature, a similar reinforcing effect is still observed as evidenced by the increase of the modulus value from 52.1 to 121.4 MPa for the 9%CNC sample.

The variation of the mechanical damping factor (or  $\tan \delta$ ) is shown in Figure 6b. The glass transition ( $\alpha$ -transition) temperature is taken as the temperature of the peak of  $\tan \delta$  curve. For the MA-g-PBAT sample, the temperature is found to be −24.3 °C  $\pm$  1.1 °C. Interestingly, with addition of cellulose nanocrystals, this transition temperature is shifted toward higher temperature where, for the 9%CNC nanocomposite sample, a transition temperature of −17.3 °C  $\pm$  1.2 °C was observed. This positive shift of the  $T_g$  is a clear indication that the presence of the CNC whiskers significantly restricts the molecular motion of the PBAT chains in the glass–rubber transition region.

This effect is indeed, enhanced by the strong interfacial adhesion in the reactive system. It should also be noted that the second (minor) transition temperature does not show any noticeable change with the addition of nanocrystals, suggesting that the impact of the CNC on chain motion restriction is significantly more prominent in the case of more flexible butylene-adipate units in comparison to the relatively stiffer phenylene segment.

In addition, as seen in the Table 4, the height of the  $\tan \delta$  peak ( $\tan \delta_{\max}$ ) reduces with increasing nanocrystal concentration. The height of the  $\tan \delta$  is associated with the energy dissipation ability of the material which is inversely related to the material elasticity. As expected, the presence of highly elastic cellulose whiskers and the enhanced elasticity of the matrix due to the interaction with the particles reduced the energy dissipation of the system. This reduction in energy dissipation is facilitated by the already described relatively



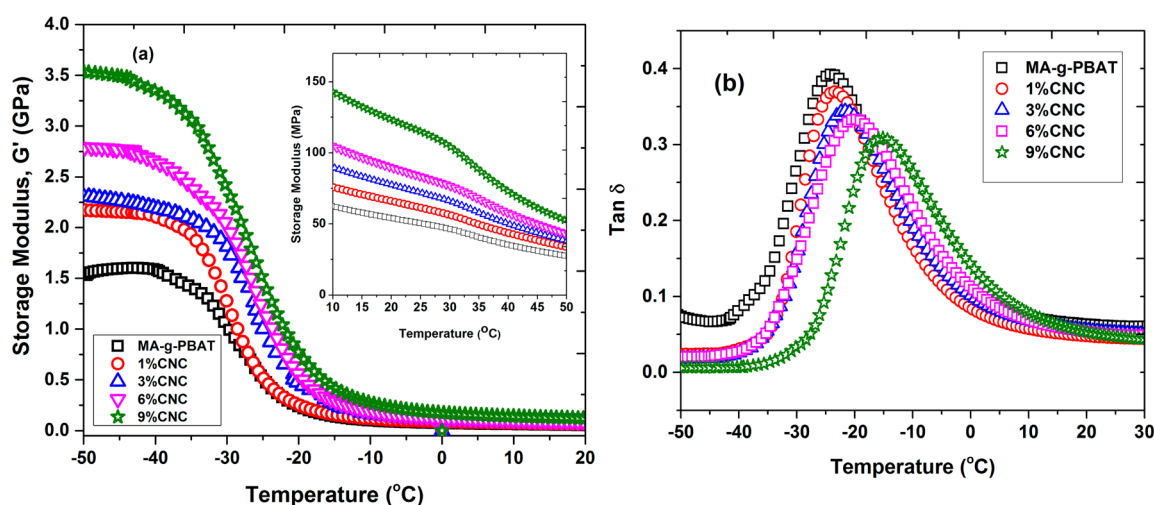


Figure 6. (a) Variation of storage modulus ( $E'$ ) vs temperature and (b)  $\tan \delta$  vs temperature.

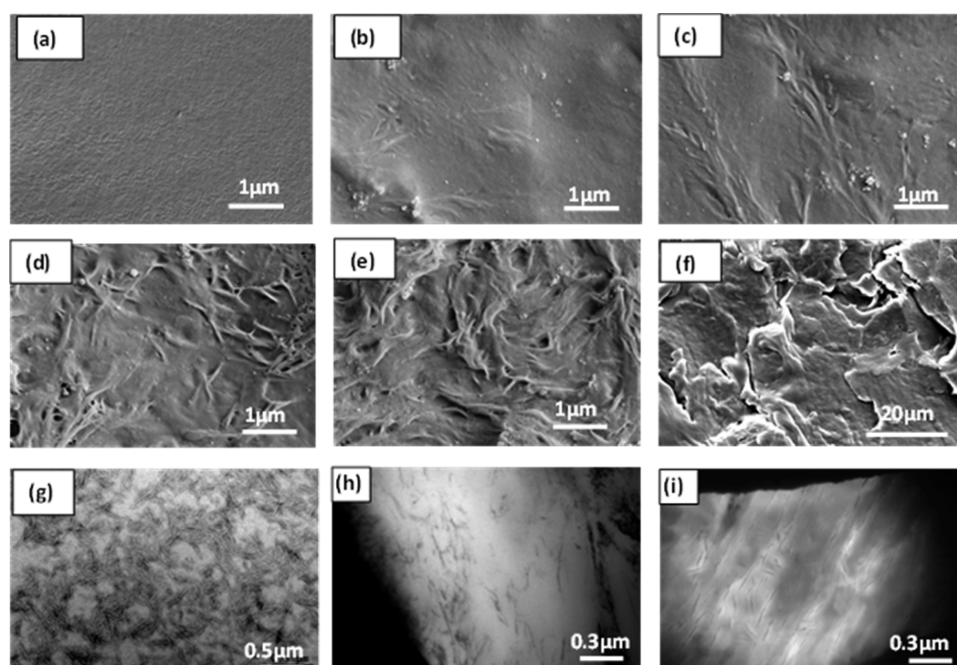


Figure 7. SEM images of cryo-fractured surfaces of (a) MA-g-PBAT, (b) 1% CNC, (c) 3% CNC, (d) 6% CNC, (e) 9% CNC, and (f) neat PBAT/9% CNC and TEM images of (g) cellulose nanocrystals, (h) 3% CNC, and (i) 9% CNC nanocomposites.

strong polymer–particle interaction, especially at high CNC concentrations.

### 3.3. Morphology and Static Mechanical Properties.

The SEM images of the cryo-fractured surfaces of the neat MA-g-PBAT matrix, the nanocomposite samples, as well as, the TEM image of the cellulose nanocrystals used in this study are shown in Figure 7. The CNCs have an average aspect ratio (i.e., length/diameter ratio) of approximately 20. The SEM images showed that the cellulose nanocrystals are mostly dispersed in submicron-sized bundles. No significant CNC particle aggregation was observed in the highest CNC concentration. In addition, the whiskers are mostly wrapped by the interfacial polymer layer (instead of being neatly pulled out after cryo-factoring), confirming a strong interfacial adhesion between the particles and matrix. Further, there is a clear increase of surface roughness as the CNC content is increased within the matrix. For the purpose of comparison, the SEM image of a control

sample with the unmodified PBAT and 9% CNC is also presented in Figure 7f, showing clearly that the CNCs formed large agglomerates in the hydrophobic matrix similar to the observation of the macro-phase separation of the molded samples. In addition, the TEM images of the 3% and 9% CNC samples shown in Figure 7h,i clearly shows that the CNC is finely dispersed in the matrix in the form of individual bundles or submicron sized bundles of whiskers.

The tensile tests results are shown in Figure 8 and Table 5. The neat MA-g-PBAT matrix shows a tensile modulus and strength at break of 50 and 16 MPa, respectively. With addition of the cellulose nanocrystals, it was observed that not only the Young's modulus of the specimens increased up to 108 MPa showing more than 100% increases, the stress at break of the samples also showed an increasing trend with increasing CNC concentration reaching a maximum value of 20 MPa with 9% CNC (i.e., nearly 25% increase in the strength). In contrast, in a

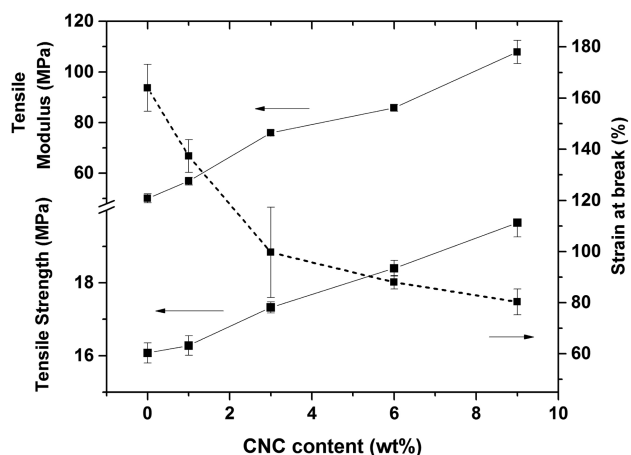


**Figure 8.** Variation of modulus, stress at break, and strain at break of MA-g-PBAT/CNC nanocomposites.

**Table 5. Mechanical Properties of MA-g-PBAT/CNC Nanocomposites**

sample	$E$ (MPa)	max. stress (MPa)	max. strain (%)
MA-g-PBAT	$50.1 \pm 1.7$	$16.1 \pm 0.3$	$164.1 \pm 9.1$
1%CNC	$56.9 \pm 1.5$	$16.3 \pm 0.3$	$157.3 \pm 6.4$
3%CNC	$76.1 \pm 0.46$	$17.4 \pm 0.1$	$99.7 \pm 17.7$
6%CNC	$85.8 \pm 1.3$	$18.6 \pm 0.2$	$88.1 \pm 2.6$
9%CNC	$107.9 \pm 4.6$	$19.7 \pm 0.4$	$80.3 \pm 4.0$

study by Zhang and co-workers,<sup>43</sup> the surface acetylation of CNC was also shown to improve the dispersion of particles in

the PBAT matrix which improved the elastic modulus of the samples.

However, the ultimate strength of the nanocomposites showed a decreasing trend with respect to CNC concentration, suggesting that the particles did not optimally reinforce the samples.

In the nanocomposites systems of the current study, the enhancement of the stress at break shows the true reinforcing ability of cellulose nanocrystals (as opposed to the study by Zhang et al.,<sup>42</sup> as mentioned above) in the PBAT matrix due to the strong interfacial adhesion that facilitates the efficient stress transfer from the polymer matrix to the CNC particles. The strain at break of the samples showed a decreasing trend with addition of the cellulose nanocrystals as Figure 8 shows.

This is in fact due to the increased elasticity of the samples which, in turn, reduced the elongation at break. In addition to the enhanced elasticity of the samples due to the presence of CNCs, formation of cross-linked structures at the polymer–CNC interface, further limits the chain slippage and drawing behavior of PBAT matrix, thereby reducing the strain at break values.

**3.4. Melt Rheological Properties.** The frequency dependencies of storage and loss moduli of the MA-g-PBAT/CNC nanocomposites at 140 °C are shown in Figure 9a,b. It can be seen from this figure that the addition of cellulose whiskers gave a significant effect on the viscoelastic properties of the matrix. Both the storage ( $G'$ ) and loss ( $G''$ ) moduli increased upon incorporation of cellulose nanocrystal particles.

This increase is, however, more noticeable at the lower frequency region. It is well-known that the rheological

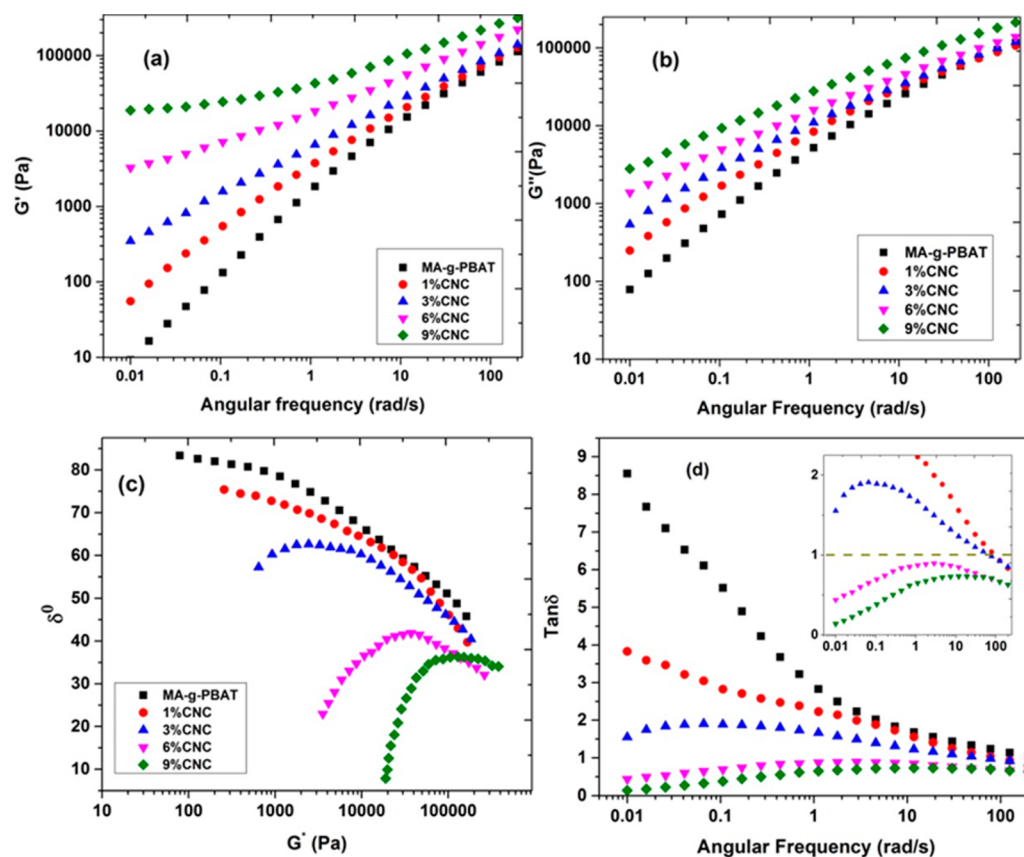


**Figure 9.** Variation of (a) storage modulus, (b) loss modulus vs frequency, (c) Van-Gurp Palmen plot, and (d) variation of  $\tan \delta$  vs frequency.

properties of polymer systems at high frequency is dominated by the short-range chain motion and relaxation process while in the low frequency zone the behavior is dictated by large-scale chain motion. In fact, at low frequencies, polymer chains exhibit the characteristics of fully relaxed chains, showing a terminal behavior that is characterized by the power law relations of  $G'' \sim \omega$  and  $G' \sim \omega^2$ .<sup>44</sup> However, as shown in Table 6, the

**Table 6. Terminal Region Slopes of Storage and Loss Modulus and Plateau Modulus of the Nanocomposites Obtained from Rheological Data**

sample	terminal slope of $G'$	terminal slope of $G''$	$G_p$ (Pa)
MA-g-PBAT	1.16	0.98	9
1%CNC	0.96	0.87	55
3%CNC	0.64	0.73	348
6%CNC	0.32	0.59	3267
9%CNC	0.11	0.55	18787

nanocomposite materials showed completely different behavior in this terminal zone. It was observed that the slope of the terminal zone of  $G'$  in the matrix is 1.16 which is reduced to 0.96 with addition of 1%CNC, and further significantly reduced to 0.11 in the case of 9%CNC. Similarly, the terminal slope of the  $G''$  curves changed from 0.98 in the matrix to 0.55 in the 9%CNC nanocomposite.

This reduction of the slope and reduced dependency of storage and loss modulus on the frequency (or development of the “non-terminal” behavior in the nanocomposites systems) is attributed to the development of the network-like interconnected nanostructure of the cellulose whiskers in the matrix. This network structure develops at higher CNC concentrations above the percolation threshold where the particle–particle and polymer–particle interactions dominate the rheological behavior of the sample, resulting in a pseudosolid-like melt behavior. In addition, it can be seen that for the 3%CNC sample, there is a crossover point between the  $G'$  and  $G''$  values in the low frequency region which is attributed to the point where the particles start to interact like others researchers have reported for somewhat similar systems.<sup>45,46</sup> However, for the 6 and 9% CNC samples, the  $G'$  values dominate the  $G''$  values across the entire frequency range studied, showing that these samples are effectively behaving like elastic melts.

In order to further correlate the microstructure of the nanocomposites with the observed rheological behavior, the fractal model of elastic colloidal gels developed by Shih et al.<sup>47</sup> was applied to interpret the experimental results. According to this theory, a closely packed arrangement of fractal “flocs” is proposed to be connected throughout the matrix material above the gelation (percolation) threshold. Depending on the floc size, weak-link regime and strong-link regime were proposed. Because in the current nanocomposite systems, the threshold of nonlinearity in the strain sweep experiments (performed prior to frequency sweep tests) characterized by the critical strain value ( $\gamma_c$ ) reduced with increasing floc concentration (or CNC content), a strong-link regime is applicable. Using the polymer solution scaling theory the following correlations were suggested:

$$G_p \sim \varphi^{(D+x)/(D-d_f)} \quad (4)$$

$$\gamma_c \sim \varphi^{-(1+x)/(D-d_f)} \quad (5)$$

where the  $G_p$  is the plateau modulus (considered here to be that at  $\omega = 0.01$  rad/s),  $D$  is the Euclidean dimension of the system (i.e.,  $D = 3$  for the current system),  $x$  is scaling power correlating the number of particles per floc with floc size, and  $d_f$  is the fractal dimension (or filler network). In the current system of this study, the flocs are considered to be composed of bundles of cellulose whiskers and the fractal network is formed by elastic linkage of these bundles (or flocs). A linear regression analysis of the data points above the percolation threshold gave a  $d_f$  value of 1.65. In a study by Durmus et al.<sup>48</sup> on polymer/clay nanocomposites, it was found that enhancing the polymer–clay interfacial adhesion reduced the fractal dimension from 2.32 to 2.17, which resulted in relatively more exfoliated structures (better dispersion). In addition, a value of 1.7 was found in a polypropylene/nanocellulose composite with web-like structure.<sup>12</sup> The value of 1.65 found in the current nanocomposite system of this study indicates a 3D web-like and porous open fractal structure.

It is worthy to note that the formation of a network-like percolated structure of CNC within the PBAT matrix can be studied by using the Van Gorp-Palmen (VGP) plot as shown in Figure 9c. In this plot, the variation of the phase angle ( $\delta^\circ$ ) is plotted against the complex modulus values obtained from the dynamic frequency sweep experiments. The evolution of the structure within the matrix could be traced by variation of the phase angle as the complex viscoelastic material functions values are decreased. It is seen, for example, that in the case of the MA-g-PBAT and 1%CNC nanocomposite, with decreasing  $G^*$  values, the phase angle monotonically increased in the direction of the full  $90^\circ$  phase angle (i.e., viscous behavior). On the other hand, for the 3%CNC sample, it can be seen that a maximum point is reached and, upon further reduction of  $G^*$ , the phase angle is also reduced. A relatively more significant deviation from the monotonic change just mentioned is also seen for the 6% and 9% CNC samples. The evolution of the curve maximum on the VGP plot has been attributed to the structural changes linked to the development of the elastic percolated structure in the melt as opposed to the behavior of the melt from purely viscous (full chain relaxation) at low frequencies.

Additionally, the variation of  $\tan \delta$  with angular frequency is shown in Figure 9d. Typically, the transition from liquid-like to solid-like behavior occurs at the crossover of the  $G'$  and  $G''$ , where  $\tan \delta = 1$ . The inverse of the frequency at which this transition point occurs is considered as the relaxation time of the polymer chains. For the PBAT/CNC systems, it is evident that with decreasing frequency, the  $\tan \delta$  values constantly increased to higher values crossing the  $\tan \delta = 1$  point at certain frequencies. By contrast, for the 1 and 3%CNC samples, this crossover occurred at lower frequencies, suggesting relatively longer relaxation times. In the case of the 3%CNC samples, upon further decreasing the frequency, it can be seen that there is a downward shift where the  $\tan \delta$  reaches a maximum and follows a decreasing trend. This shows that for this sample, there are some elastic contributions in the low frequency region that reduce the viscous character of the polymer melt and, thus, decrease the  $\tan \delta$  value. This observation is attributed to the onset of percolated network structure formation. Further increasing the CNC concentration to 6 and 9% resulted in  $\tan \delta$  values being constantly less than the  $\tan \delta = 1$  threshold, suggesting that these samples are effectively behaving like an elastic fluid.



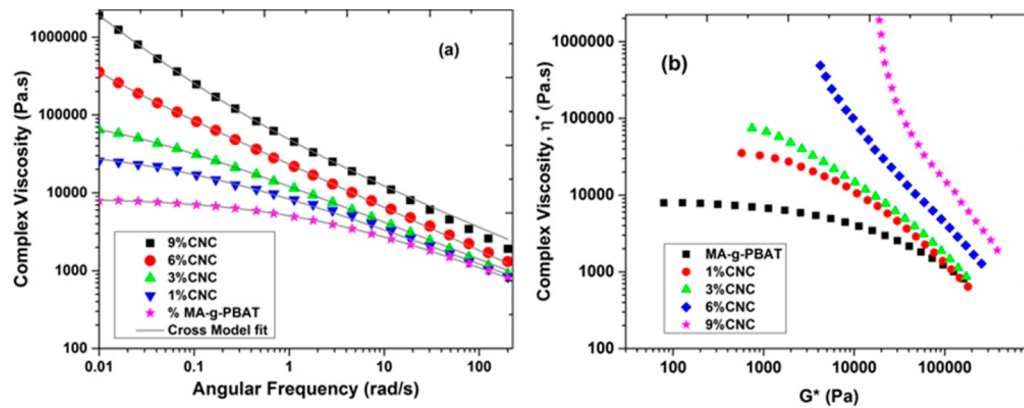


**Figure 10.** Variation of (a) complex viscosity versus frequency and (b) complex viscosity vs complex modulus.

The variation of the complex viscosity ( $\eta^*$ ) versus angular frequency is shown in Figure 10a. Incorporation of the CNC particles to the MA-g-PBAT matrix monotonically increased the viscosity of the samples throughout the studied frequency range.

There is, however, a noticeable upward shift in the viscosity values at low frequencies as the CNC concentration increased. This effect is more noticeable in the case of 6 and 9% CNC samples. This upward shift in data is a nanostructure formation signature and indicates an apparent yield stress in the samples.

This effect is also observed in Figure 10b where complex viscosity is plotted against complex modulus. In the case of the 3% CNC nanocomposite, there is an upward shift in the complex viscosity at low complex modulus values while this shift is significantly increased for the 6 and 9% CNC samples. This behavior has been reported for polymer systems that are highly filled with microparticles.<sup>49</sup> The development of the nonterminal characteristic associated with this observed yield stress is attributed to the network-like structure formation above the 3% concentration of CNCs. In order to further investigate this behavior and to calculate the yield stress values, the modified Cross model<sup>12</sup> that includes a yield stress term was applied to the experimental data according to the following equation:

$$\eta = \sigma_y \cdot \omega^{-1} + \eta_p (1 + \alpha \omega^m)^{-1} \quad (6)$$

where the  $\eta_p$  (Pa·s),  $\alpha$  (s), and  $m$  are the model fit parameters. The results of the Cross model fitting to the experimental data are shown in Table 7.

**Table 7.** Fit Parameters of Cross Model

sample	$\sigma_y$ (Pa)	$\eta_p$ (Pa·s)	$\alpha$ (S)	$m$
MA-g-PBAT		8622.6	0.69	0.49
1%CNC	41.3	38800	3.27	0.57
3%CNC	741.7	39425.1	2.2	0.61
6%CNC	2616.4	329255.3	11.8	0.56
9%CNC	17161.8	406697.4	12.9	0.50

It can be seen from this table that, while the neat matrix does not show any yield stress behavior, the nanocomposite samples showed yield stress values that increased with increasing CNC concentration up to the value of 17 kPa for the 9% CNC concentration. As already discussed, the formation of the interconnected network structure above the percolation threshold within the sample may be attributed to the formation

of flocs which, in the current system, is composed of CNC bundles that are above the percolation threshold that form interconnected structures. The characteristic size of these flocs can be estimated using the obtained yield stress values. Assuming that the 3D network is composed of spheres with a random distribution and  $N$  number of CNC particles are encapsulated within the spheres with a volume of  $V_p$ .<sup>50</sup> The percolation threshold of the overlapping spheres with random packing arrangement occurs at the volume fraction of 0.32. Thus, the volume fraction of CNC within each sphere can be written as

$$\varphi = \frac{0.32NV_p}{4\pi r^3/3} \quad (7)$$

According to the Rumpf's theory of strength of granular materials and aggregates,<sup>51</sup> the strength of an aggregate can be written as

$$\sigma_T = \frac{1 - \varepsilon}{\varepsilon} \frac{A_H}{\frac{3}{2}\pi z_0^2 d} \quad (8)$$

where the  $\varepsilon$  is the porosity of the spherical units ( $= 1 - \varphi/0.32$ ),  $A_H$  is the Hamaker constant,  $z_0$  is the cutoff distance, and  $d$  is the effective agglomerate diameter. The Hamaker constant is calculated by  $A_H = 2\pi z_0^2 \gamma$ , where  $\gamma$  is the surface energy of the cellulose nanocrystals taken as 18.6 mJ/m<sup>2</sup>.<sup>52</sup> In the current system, it is assumed that upon yielding, the yield stress overcomes the strength of the aggregates (i.e.,  $\sigma_T = \sigma_y$ ). Finally, the effective aggregate diameter can be found by the inverse of the slope of the linear regression of the following equation:

$$\sigma_y = \left( \frac{1 - \varepsilon}{\varepsilon} \right) \frac{4}{3\gamma} \times \left( \frac{1}{d} \right) \quad (9)$$

For each volume fraction of the CNC, the yield stress is plotted against the  $\left( \frac{1 - \varepsilon}{\varepsilon} \right)$ . The calculated aggregate diameter was found to be 334 nm. This value is in a reasonable agreement with the value of 102 nm found in a previous study on polypropylene/CNC nanocomposite systems.<sup>12</sup>

In summary of this section, it is worth noting that in the current nanocomposite materials, the evolution of the pseudosolid-like behavior above the percolation threshold is the result of the particle–particle interactions. However, the “bridging” effect of the interfacial polymer layers should not be neglected. As already shown in the  $\tan \delta$  plot, the relaxation time of the polymer increased with increasing the CNC content. This increase in relaxation time may in fact be related

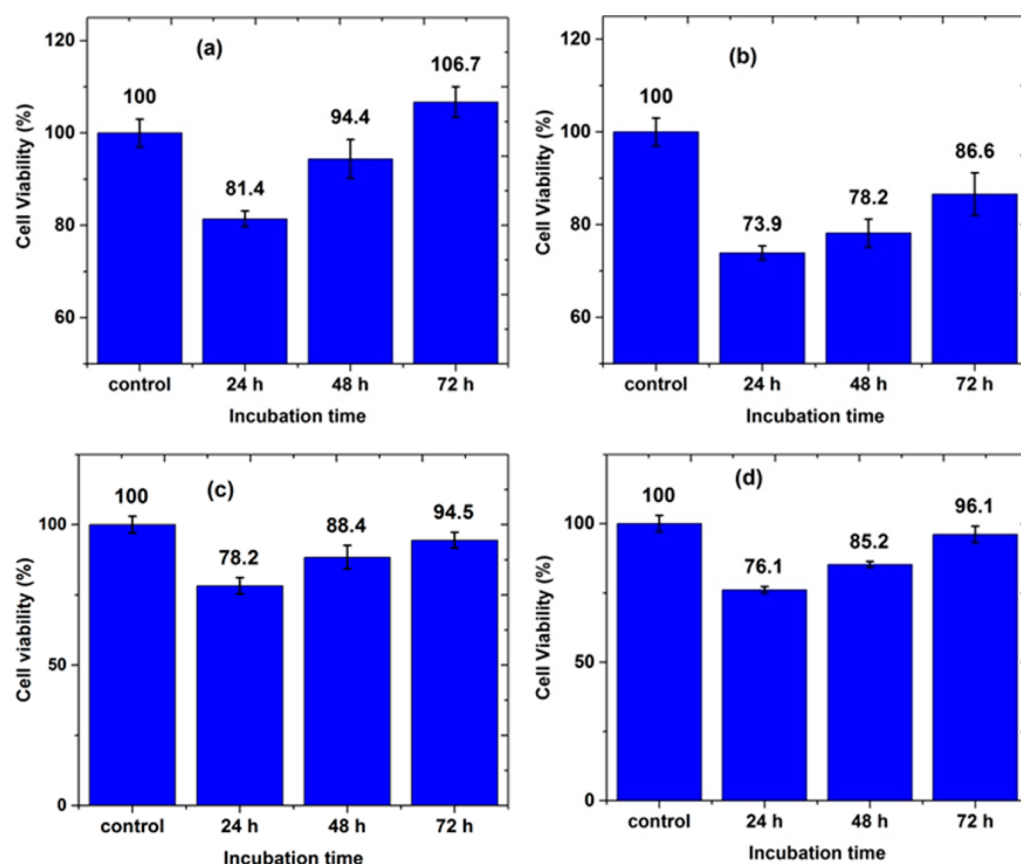


**Figure 11.** MTT assay cell viability of L929 cells for (a) MA-g-PBAT, (b) CNC, (c) 3%CNC, and (d) 9%CNC samples at specified incubation times.

to the development of the constrained polymer layer in contact with CNC particles due to the strong interfacial adhesion. This “rigid interphase” has been shown in a number of previous studies,<sup>17</sup> especially in cases where strong interfacial interaction exists, to effectively increase the volume fraction of the “rigid phase”, thus, lowering the effective percolation threshold.

**3.5. In Vitro Biocompatibility Studies.** Cellulose nanocrystals have been shown in a number of previous publications in the literature to be generally biocompatible with no significant cytotoxicity.<sup>53</sup> In a study by Dong et al.,<sup>54</sup> the cytotoxicity of cellulose nanocrystals were studied against a range of cell lines including human brain microvascular endothelial cells (HBMEC), KB cells, prostate cancer (PC-3), C6 stem cells, and breast cancer cell (MDA-MB) using MTT and LDH assays in the concentration range of 0–50  $\mu\text{g/mL}$  and exposure time of 48 h, and no noticeable cytotoxic effect was observed in any of the systems studied. In addition, a number of different polymer nanocomposites reinforced with cellulose nanocrystals, such as polyurethanes,<sup>55</sup> collagen,<sup>56</sup> and polylactic acid,<sup>57</sup> have been evaluated to show favorable biocompatible properties with improved cell proliferation and adhesion. On the other hand, a number of studies have reported a concentration dependency of cytotoxicity of CNC in selected culture media where no (or little) cytotoxic effect was observed against various cell lines up to a concentration of 250  $\mu\text{g/mL}$ .<sup>58</sup>

Because a number of PBAT-based composite materials have been used for tissue engineering and biomedical applications,<sup>24</sup> the current system of PBAT reinforced with cellulose nanocrystals shows a promising potential for such application.

Therefore, the cell response and cell adhesion properties of the nanocomposites were studied to assess its viability in the applications just mentioned.

Here, fibroblast L929 cell line was chosen for the MTT assay analysis because it has been recommended by the International Standard Organization (ISO) as the cell line for in vitro MTT assay test.<sup>59</sup> The MTT assay is based on reduction of tetrazolium compound by a functioning mitochondria into a nonsoluble purple formazan precipitate that accumulates in the culture medium and can be assessed calorimetrically to quantify the number of living cells. The quantitative results of MTT assay cell viability tests for PBAT/CNC nanocomposites with 3 and 9%CNC after incubation periods of 24, 48, and 72 h are presented in Figure 11. Additionally, a sample of the CNC in the culture medium was also tested as “control” sample. The concentration of CNC was chosen as 50  $\mu\text{g/mL}$  to prevent particle aggregation and interference during the MTT assay tests.<sup>60</sup>

The obtained results showed that all the samples including the CNC dispersion gave no sign of cytotoxicity against L929 fibroblast cells as evidenced by the experimental fact that they all had cell growth rates of above 30% which is considered to be the threshold for cytotoxicity.<sup>61</sup> For all the samples, the viability of the L929 cells increased monotonically with increasing culture times. It is clear from these results that all the nanocomposite samples are biocompatible and no samples showed observable cytotoxicity. In addition, the cellulose nanocrystals did not show cytotoxic effect at the studied concentrations as evidenced by the cell growth rate over the 72 h period. Moreover, there is no significant difference in the

viability of the samples albeit the neat MA-g-PBAT showed a slightly higher proliferation compared to that of the nanocomposite samples, especially in the first 2 days of the incubation time. The optical micrograph showing the cell viability of the 9%CNC sample at the beginning and after 72 h of culture is presented in Figure 12. As can be seen in this figure, the cells significantly populated the sample after 72 h which is in agreement with the results of the cell proliferation assay.

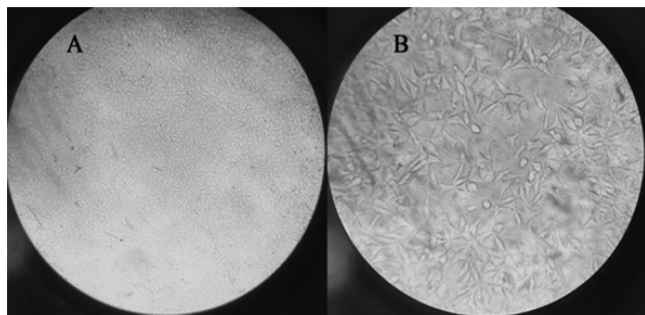


**Figure 12.** L929 cell proliferation on 9%CNC nanocomposite at (a) 0 h and (b) 48 h of incubation time ( $\times 10$ -fold magnification).

The adhesion of the fibroblast cells on the MA-g-PBAT and 9%CNC samples after 72 h of incubation are shown in Figure 13. In both samples the surface of the specimen is massively

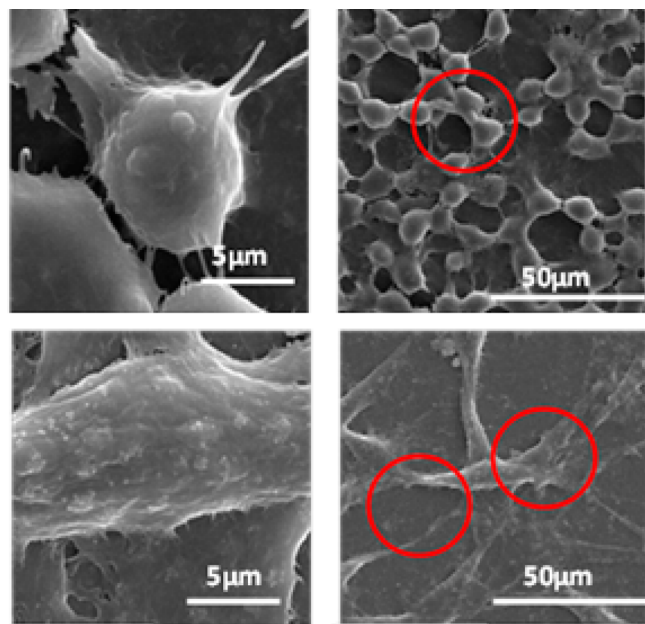


**Figure 13.** SEM images showing the L929 cell adhesion and growth on (top) MA-g-PBAT and (bottom) 9%CNC nanocomposite after 72 h of culture.

colonized by the cells where they proliferated and were adhered very well, confirming the L929 cell viability of both the matrix and the nanocomposite sample.

More interestingly, the morphology of the cells on the surface of the MA-g-PBAT sample showed a spindle-like shape of the cells while in the case of the nanocomposite sample, the cells are much more flat with a spread-out web-like structure on the surface with more clear pseudopods that showed a better intercellular connection. Note that a number of different

surface characteristics can affect the cell adhesion such as topography, surface charge and specific interaction.<sup>62</sup>

An important factor for the current observation in this study is attributed to the significantly enhanced surface roughness of the nanocomposites samples due to the presence of CNC bundles (which was evident from the SEM images of the nanocomposite surface in Figure 7 already discussed).

It is worthy to note that enhancement of cell adhesion has been shown to significantly increase with increased surface roughness of the substrates.<sup>63</sup> In a study by Palin et al.,<sup>62</sup> it was shown that mimicking the surface roughness of bone with creation of surface “nano-features” using ceramic nanoparticles significantly enhanced the osteoblast cell adhesion on the synthetic mold. In another study,<sup>64</sup> it was shown that coating the melt-drawn polylactic acid fibers with cellulose whiskers resulted in significant improvement of NIH-3T3 cell adhesion on the fibers due to enhanced surface roughness of the fibers. In addition, the effect of the presence of nanostructure with high porosity on promotion of cell differentiation and proliferation of polymer-based nanocomposites was demonstrated in our previous publication<sup>65,66</sup> in polyurethane/POSS nanocomposites. In the current study, the observed porous nanostructure of nanocrystals within the matrix enhanced the cell adhesion by mimicking the extracellular matrix topology.

In addition to the surface roughness, it is believed that the enhanced surface hydrophilicity of the nanocomposites compared to that of the matrix due to the presence of the cellulose whiskers with hydroxyl group-rich surfaces played a critical role in improving the cell adhesion and development of intercellular connections.

The critical role of the surface functionality and wettability on cell adhesion was shown in the work of Arima and co-workers<sup>67</sup> who reported maximum cell adhesion on artificial surfaces of self-assembled monolayers functionalized with hydroxyl (–OH) and carboxyl (–COOH) groups with low water contact angle (i.e., high wettability). In the current PBAT/CNC nanocomposite system, it is believed that the synergistic effect of both the enhanced surface roughness and higher surface energy of the nanocomposite samples are responsible for the observed cell adhesion and growth on the sample surface.

#### 4. CONCLUSIONS

In this study, a series of MA-g-PBAT/CNC nanocomposites with 1,3,6 and 9 wt % of CNC were prepared by first modifying the PBAT polymer with maleic anhydride groups via free radical grafting followed by reactive extrusion processing of the MA-g-PBAT with cellulose nanocrystals (CNCs). The molecular characterization results obtained from <sup>1</sup>H NMR and ATR-IR spectroscopy confirmed the grafting of the MA onto the PBAT chains, as well as, the possible associated structural changes. Thermal characterization of the nanocomposites showed thermal stability improvement of the materials as the CNC content increased. In addition, it was found that the CNCs promoted crystallization of the PBAT due to the heterogeneous nucleation effect. The analysis of the mechanical properties of the samples showed a significant improvement in the elastic modulus of the PBAT (i.e., up to 114% increase with 9% of CNC) as well as a 25% increase in the ultimate tensile strength. Dynamic mechanical analysis results showed that upon introducing the CNCs into the modified PBAT matrix, the  $T_g$  of the matrix shifted toward higher temperature, indicative of the PBAT chain motion



restriction effect of CNCs. This effect was further investigated using melt rheological studies where it was found that the viscoelastic material functions of the PBAT showed a monotonous increase with increasing CNC content while the observed development of the nonterminal behavior suggested the evolution of the 3D web-like percolated network of CNC within the matrix above 3% CNC. The *in vitro* cytotoxicity evaluation of the nanocomposites showed no cytotoxic effect, confirming the biocompatibility of these nanocomposites. In addition, the morphological observation of the cultured surfaces showed an enhanced cell adhesion for the 9% CNC nanocomposite compared to that of the MA-g-PBAT matrix due to alteration of the surface properties which favors the cell differentiation.

## ■ ASSOCIATED CONTENT

### ■ Supporting Information

The Supporting Information is available free of charge on the ACS Publications website at DOI: [10.1021/acs.biomac.7b00578](https://doi.org/10.1021/acs.biomac.7b00578).

<sup>1</sup>H NMR spectra of PBAT and MA-g-PBAT. TGA and DTG plots of unmodified PBAT/CNC nanocomposites. Rheological properties (storage modulus, loss modulus, and complex viscosity as a function of frequency) of unmodified PBAT/CNC nanocomposites (PDF).

## ■ AUTHOR INFORMATION

### Corresponding Author

\*E-mail: [joshua.otaigbe@usm.edu](mailto:joshua.otaigbe@usm.edu). Phone: (601) 266-5596. Fax: (601) 266-5504.

### ORCID

Joshua U Otaigbe: [0000-0003-3565-6571](https://orcid.org/0000-0003-3565-6571)

### Notes

The authors declare no competing financial interest.

## ■ ACKNOWLEDGMENTS

The financial support by the U.S. National Science Foundation Division of Civil, Mechanical and Manufacturing Innovation through CMMI-1161292 grant award is gratefully acknowledged. The authors are grateful to Jessica Douglas at the School of Polymers and High Performance Materials of The University of Southern Mississippi for assistance with TEM and SEM imaging.

## ■ REFERENCES

- Habibi, Y.; Lucia, L. A.; Rojas, O. J. Cellulose nanocrystals: chemistry, self-assembly, and applications. *Chem. Rev.* **2010**, *110* (6), 3479–3500.
- Moon, R. J.; Martini, A.; Nairn, J.; Simonsen, J.; Youngblood, J. Cellulose nanomaterials review: structure, properties and nanocomposites. *Chem. Soc. Rev.* **2011**, *40* (7), 3941–3994.
- Mariano, M.; El Kissi, N.; Dufresne, A. Cellulose nanocrystals and related nanocomposites: review of some properties and challenges. *J. Polym. Sci., Part B: Polym. Phys.* **2014**, *52* (12), 791–806.
- Salas, C.; Nypelö, T.; Rodriguez-Abreu, C.; Carrillo, C.; Rojas, O. J. Nanocellulose properties and applications in colloids and interfaces. *Curr. Opin. Colloid Interface Sci.* **2014**, *19* (5), 383–396.
- Feese, E.; Sadeghifar, H.; Gracz, H. S.; Argyropoulos, D. S.; Ghiladi, R. A. Photobactericidal porphyrin-cellulose nanocrystals: synthesis, characterization, and antimicrobial properties. *Biomacromolecules* **2011**, *12* (10), 3528–3539.
- Belbekhouche, S.; Bras, J.; Siqueira, G.; Chappey, C.; Lebrun, L.; Khelifi, B.; Marais, S.; Dufresne, A. Water sorption behavior and gas barrier properties of cellulose whiskers and microfibrils films. *Carbohydr. Polym.* **2011**, *83* (4), 1740–1748.
- Tingaut, P.; Zimmermann, T.; Sèbe, G. Cellulose nanocrystals and microfibrillated cellulose as building blocks for the design of hierarchical functional materials. *J. Mater. Chem.* **2012**, *22* (38), 20105–20111.
- Peresin, M. S.; Habibi, Y.; Zoppe, J. O.; Pawlak, J. J.; Rojas, O. J. Nanofiber composites of polyvinyl alcohol and cellulose nanocrystals: manufacture and characterization. *Biomacromolecules* **2010**, *11* (3), 674–681.
- Liu, H.; Liu, D.; Yao, F.; Wu, Q. Fabrication and properties of transparent polymethylmethacrylate/cellulose nanocrystals composites. *Bioresour. Technol.* **2010**, *101* (14), S685–S692.
- Kashani Rahimi, S.; Otaigbe, J. U. Polyamide 6 nanocomposites incorporating cellulose nanocrystals prepared by *In situ* ring-opening polymerization: Viscoelasticity, creep behavior, and melt rheological properties. *Polym. Eng. Sci.* **2016**, *56* (9), 1045–1060.
- Goffin, A.-L.; Raquez, J.-M.; Duquesne, E.; Siqueira, G.; Habibi, Y.; Dufresne, A.; Dubois, P. Poly( $\epsilon$ -caprolactone) based nanocomposites reinforced by surface-grafted cellulose nanowhiskers via extrusion processing: morphology, rheology, and thermo-mechanical properties. *Polymer* **2011**, *52* (7), 1532–1538.
- Khoshkava, V.; Kamal, M. R. Effect of cellulose nanocrystals (CNC) particle morphology on dispersion and rheological and mechanical properties of polypropylene/CNC nanocomposites. *ACS Appl. Mater. Interfaces* **2014**, *6* (11), 8146–8157.
- Favier, V.; Dendievel, R.; Canova, G.; Cavaille, J.; Gilormini, P. Simulation and modeling of three-dimensional percolating structures: case of a latex matrix reinforced by a network of cellulose fibers. *Acta Mater.* **1997**, *45* (4), 1557–1565.
- Cao, X.; Dong, H.; Li, C. M. New nanocomposite materials reinforced with flax cellulose nanocrystals in waterborne polyurethane. *Biomacromolecules* **2007**, *8* (3), 899–904.
- Roohani, M.; Habibi, Y.; Belgacem, N. M.; Ebrahim, G.; Karimi, A. N.; Dufresne, A. Cellulose whiskers reinforced polyvinyl alcohol copolymers nanocomposites. *Eur. Polym. J.* **2008**, *44* (8), 2489–2498.
- Pereda, M.; Amica, G.; Rácz, I.; Marcovich, N. E. Structure and properties of nanocomposite films based on sodium caseinate and nanocellulose fibers. *J. Food Eng.* **2011**, *103* (1), 76–83.
- Tang, L.; Weder, C. Cellulose whisker/epoxy resin nanocomposites. *ACS Appl. Mater. Interfaces* **2010**, *2* (4), 1073–1080.
- Gupta, A.; Kumar, V. New emerging trends in synthetic biodegradable polymers—Polylactide: A critique. *Eur. Polym. J.* **2007**, *43* (10), 4053–4074.
- Shi, X.; Ito, H.; Kikutani, T. Characterization on mixed-crystal structure and properties of poly (butylene adipate-co-terephthalate) biodegradable fibers. *Polymer* **2005**, *46* (25), 11442–11450.
- Kijchavengkul, T.; Auras, R.; Rubino, M.; Alvarado, E.; Montero, J. R. C.; Rosales, J. M. Atmospheric and soil degradation of aliphatic-aromatic polyester films. *Polym. Degrad. Stab.* **2010**, *95* (2), 99–107.
- Averous, L.; Le Digabel, F. Properties of biocomposites based on lignocellulosic fillers. *Carbohydr. Polym.* **2006**, *66* (4), 480–493.
- Fukushima, K.; Rasyida, A.; Yang, M.-C. Biocompatibility of organically modified nanocomposites based on PBAT. *J. Polym. Res.* **2013**, *20* (11), 302.
- Al-Itry, R.; Lamnawar, K.; Maazouz, A. Improvement of thermal stability, rheological and mechanical properties of PLA, PBAT and their blends by reactive extrusion with functionalized epoxy. *Polym. Degrad. Stab.* **2012**, *97* (10), 1898–1914.
- Fukushima, K.; Wu, M.-H.; Bocchini, S.; Rasyida, A.; Yang, M.-C. PBAT based nanocomposites for medical and industrial applications. *Mater. Sci. Eng., C* **2012**, *32* (6), 1331–1351.
- Hong, S.; Ko, S.; Choi, H.; Lee, J. Multi-walled carbon nanotube/biodegradable poly (butyleneadipate-co-butylene-terephthalate) nanocomposites and their physical characteristics. *J. Macromol. Sci., Part B: Phys.* **2012**, *51* (1), 125–133.
- Kashi, S.; Gupta, R. K.; Kao, N.; Bhattacharya, S. N., Electrical, thermal, and viscoelastic properties of graphene nanoplatelet/poly-

- (butylene adipate-co-terephthalate) biodegradable nanocomposites. *J. Appl. Polym. Sci.* **2016**, 133 (27), 10.1002/app.43620
- (27) Someya, Y.; Sugahara, Y.; Shibata, M. Nanocomposites based on poly (butylene adipate-co-terephthalate) and montmorillonite. *J. Appl. Polym. Sci.* **2005**, 95 (2), 386–392.
- (28) Mohanty, S.; Nayak, S. K. Aromatic-aliphatic poly(butylene adipate-co-terephthalate) bionanocomposite: Influence of organic modification on structure and properties. *Polym. Compos.* **2010**, 31 (7), 1194–1204.
- (29) Nabar, Y.; Raquez, J. M.; Dubois, P.; Narayan, R. Production of starch foams by twin-screw extrusion: Effect of maleated poly (butylene adipate-co-terephthalate) as a compatibilizer. *Biomacromolecules* **2005**, 6 (2), 807–817.
- (30) Rahimi, S. K.; Otaigbe, J. U. The role of particle surface functionality and microstructure development in isothermal and non-isothermal crystallization behavior of polyamide 6/cellulose nanocrystals nanocomposites. *Polymer* **2016**, 107, 316–331.
- (31) Dong, X. M.; Revol, J.-F.; Gray, D. G. Effect of microcrystallite preparation conditions on the formation of colloid crystals of cellulose. *Cellulose* **1998**, 5 (1), 19–32.
- (32) Mani, R.; Bhattacharya, M.; Tang, J. Functionalization of polyesters with maleic anhydride by reactive extrusion. *J. Polym. Sci., Part A: Polym. Chem.* **1999**, 37 (11), 1693–1702.
- (33) Bratawidjaja, A. S.; Gitopadmoyo, I.; Watanabe, Y.; Hatakeyama, T. Adhesive property of polypropylene modified with maleic anhydride by extrusion molding. *J. Appl. Polym. Sci.* **1989**, 37 (4), 1141–1145.
- (34) Carlson, D.; Nie, L.; Narayan, R.; Dubois, P. Maleation of polylactide (PLA) by reactive extrusion. *J. Appl. Polym. Sci.* **1999**, 72 (4), 477–485.
- (35) Carlson, D.; Dubois, P.; Nie, L.; Narayan, R. Free radical branching of polylactide by reactive extrusion. *Polym. Eng. Sci.* **1998**, 38 (2), 311–321.
- (36) Miyauchi, K.; Saito, K. <sup>1</sup>H NMR assignment of oligomeric grafts of maleic anhydride-grafted polyolefin. *Magn. Reson. Chem.* **2012**, 50 (8), 580–583.
- (37) Zhao, P.; Liu, W.; Wu, Q.; Ren, J. Preparation, mechanical, and thermal properties of biodegradable polyesters/poly (lactic acid) blends. *J. Nanomater.* **2010**, 2010, 4.
- (38) Weng, Y.-X.; Jin, Y.-J.; Meng, Q.-Y.; Wang, L.; Zhang, M.; Wang, Y.-Z. Biodegradation behavior of poly (butylene adipate-co-terephthalate) (PBAT), poly (lactic acid) (PLA), and their blend under soil conditions. *Polym. Test.* **2013**, 32 (5), 918–926.
- (39) Wu, C.-S. Characterization of cellulose acetate-reinforced aliphatic-aromatic copolyester composites. *Carbohydr. Polym.* **2012**, 87 (2), 1249–1256.
- (40) Kamal, M. R.; Khoshkava, V. Effect of cellulose nanocrystals (CNC) on rheological and mechanical properties and crystallization behavior of PLA/CNC nanocomposites. *Carbohydr. Polym.* **2015**, 123, 105–114.
- (41) Herrera, R.; Franco, L.; Rodríguez-Galán, A.; Puiggali, J. Characterization and degradation behavior of poly (butylene adipate-co-terephthalate)s. *J. Polym. Sci., Part A: Polym. Chem.* **2002**, 40 (23), 4141–4157.
- (42) Ten, E.; Jiang, L.; Wolcott, M. P. Crystallization kinetics of poly (3-hydroxybutyrate-co-3-hydroxyvalerate)/cellulose nanowhiskers composites. *Carbohydr. Polym.* **2012**, 90 (1), 541–550.
- (43) Zhang, X.; Ma, P.; Zhang, Y. Structure and properties of surface-acetylated cellulose nanocrystal/poly (butylene adipate-co-terephthalate) composites. *Polym. Bull.* **2016**, 73 (7), 2073–2085.
- (44) Krishnamoorti, R.; Vaia, R. A.; Giannelis, E. P. Structure and dynamics of polymer-layered silicate nanocomposites. *Chem. Mater.* **1996**, 8 (8), 1728–1734.
- (45) Litchfield, D. W.; Baird, D. G. The rheology of high aspect ratio nano-particle filled liquids. *Rheol. Rev.* **2006**, 2006, 1.
- (46) Chauve, G.; Heux, L.; Arouini, R.; Mazeau, K. Cellulose poly (ethylene-co-vinyl acetate) nanocomposites studied by molecular modeling and mechanical spectroscopy. *Biomacromolecules* **2005**, 6 (4), 2025–2031.
- (47) Shih, W.-H.; Shih, W. Y.; Kim, S.-I.; Liu, J.; Aksay, I. A. Scaling behavior of the elastic properties of colloidal gels. *Phys. Rev. A: At, Mol., Opt. Phys.* **1990**, 42 (8), 4772.
- (48) Durmus, A.; Kasgoz, A.; Macosko, C. W. Linear low density polyethylene (LLDPE)/clay nanocomposites. Part I: Structural characterization and quantifying clay dispersion by melt rheology. *Polymer* **2007**, 48 (15), 4492–4502.
- (49) Utracki, L. Flow and flow orientation of composites containing anisometric particles. *Polym. Compos.* **1986**, 7 (5), 274–282.
- (50) Ren, J.; Silva, A. S.; Krishnamoorti, R. Linear viscoelasticity of disordered polystyrene–polyisoprene block copolymer based layered-silicate nanocomposites. *Macromolecules* **2000**, 33 (10), 3739–3746.
- (51) Schilde, C. *Structure, Mechanics, and Fracture of Nanoparticulate Aggregates*; Sierke Verlag: Gottingen, 2012; Vol. 10.
- (52) Khoshkava, V.; Kamal, M. Effect of surface energy on dispersion and mechanical properties of polymer/nanocrystalline cellulose nanocomposites. *Biomacromolecules* **2013**, 14 (9), 3155–3163.
- (53) Lin, N.; Dufresne, A. Nanocellulose in biomedicine: Current status and future prospect. *Eur. Polym. J.* **2014**, 59, 302–325.
- (54) Dong, S.; Hirani, A. A.; Colacino, K. R.; Lee, Y. W.; Roman, M. Cytotoxicity and cellular uptake of cellulose nanocrystals. *Nano LIFE* **2012**, 2 (03), 1241006.
- (55) Rueda, L.; Saralegi, A.; Fernández-d'Arlas, B.; Zhou, Q.; Alonso-Varona, A.; Berglund, L. A.; Mondragon, I.; Corcuera, M.; Eceiza, A. In situ polymerization and characterization of elastomeric polyurethane-cellulose nanocrystal nanocomposites. Cell response evaluation. *Cellulose* **2013**, 20 (4), 1819–1828.
- (56) Li, W.; Guo, R.; Lan, Y.; Zhang, Y.; Xue, W.; Zhang, Y. Preparation and properties of cellulose nanocrystals reinforced collagen composite films. *J. Biomed. Mater. Res., Part A* **2014**, 102 (4), 1131–1139.
- (57) Fortunati, E.; Armentano, I.; Zhou, Q.; Iannoni, A.; Saino, E.; Visai, L.; Berglund, L. A.; Kenny, J. Multifunctional bionanocomposite films of poly (lactic acid), cellulose nanocrystals and silver nanoparticles. *Carbohydr. Polym.* **2012**, 87 (2), 1596–1605.
- (58) Domingues, R. M.; Gomes, M. E.; Reis, R. L. The potential of cellulose nanocrystals in tissue engineering strategies. *Biomacromolecules* **2014**, 15 (7), 2327–2346.
- (59) Biological evaluation of medical devices, Part 5: Tests for in vitro cytotoxicity. *ISO 10993-5:2009*; ISO: Geneva, Switzerland, 1999.
- (60) Kroll, A.; Dierker, C.; Rommel, C.; Hahn, D.; Wohlleben, W.; Schulze-Isfort, C.; Göbbert, C.; Voetz, M.; Hardinghaus, F.; Schneckeburger, J. Cytotoxicity screening of 23 engineered nanomaterials using a test matrix of ten cell lines and three different assays. *Part. Fibre Toxicol.* **2011**, 8 (1), 9.
- (61) Jao, W. C.; Lin, C. H.; Hsieh, J. Y.; Yeh, Y. H.; Liu, C. Y.; Yang, M. C. Effect of immobilization of polysaccharides on the biocompatibility of poly(butylene adipate-co-terephthalate) films. *Polym. Adv. Technol.* **2010**, 21 (8), 543–553.
- (62) Palin, E.; Liu, H.; Webster, T. J. Mimicking the nanofeatures of bone increases bone-forming cell adhesion and proliferation. *Nanotechnology* **2005**, 16 (9), 1828.
- (63) Hallab, N. J.; Bundy, K. J.; O'Connor, K.; Moses, R. L.; Jacobs, J. J. Evaluation of metallic and polymeric biomaterial surface energy and surface roughness characteristics for directed cell adhesion. *Tissue Eng.* **2001**, 7 (1), 55–71.
- (64) Hossain, K. M. Z.; Hasan, M. S.; Boyd, D.; Rudd, C. D.; Ahmed, I.; Thielemans, W. Effect of cellulose nanowhiskers on surface morphology, mechanical properties, and cell adhesion of melt-drawn polylactic acid fibers. *Biomacromolecules* **2014**, 15 (4), 1498–1506.
- (65) Guo, Y. L.; Wang, W.; Otaigbe, J. U. Biocompatibility of synthetic poly (ester urethane)/polyhedral oligomeric silsesquioxane matrices with embryonic stem cell proliferation and differentiation. *J. Tissue Eng. Regener. Med.* **2010**, 4 (7), 553–564.
- (66) Wang, W.; Guo, Y.-L.; Otaigbe, J. U. The synthesis, characterization and biocompatibility of poly (ester urethane)/polyhedral oligomeric silsesquioxane nanocomposites. *Polymer* **2009**, 50 (24), 5749–5757.

(67) Arima, Y.; Iwata, H. Effect of wettability and surface functional groups on protein adsorption and cell adhesion using well-defined mixed self-assembled monolayers. *Biomaterials* **2007**, 28 (20), 3074–3082.